universität
innsbruck

Institut für Mathematik

Full field inversion in photoacoustic tomography with variable sound speed

G. Zangerl, M. Haltmeier, L. V. Nguyen, R. Nuster

APPLIEDMATHEMATICS

Full field inversion in photoacoustic tomography with variable sound speed

Gerhard Zangerl and Markus Haltmeier

Department of Mathematics, University of Innsbruck
Technikestraße 13, 6020 Innsbruck, Austria
E-mail: {gerhard.zangerl,markus.haltmeier}@uibk.ac.at

Linh V. Nguyen

Department of Mathematics, University of Idaho
875 Perimeter Dr, Moscow, ID 83844, US
E-mail: lnguyen@uidaho.edu

Robert Nuster

Department of Physics, University of Graz
Universitätsplatz 5, 8010 Graz, Austria
E-mail: ro.nuster@uni-graz.at

August 2, 2018

Abstract

Recently, a novel measurement setup has been introduced to photoacoustic tomography, that collects data in the form of projections of the full 3D acoustic pressure distribution at a certain time instant. Existing imaging algorithms for this kind of data assume a constant speed of sound. This assumption is not always met in practice and thus leads to erroneous reconstructions. In this paper, we present a two-step reconstruction method for full field detection photoacoustic tomography that takes variable speed of sound into account. In the first step, by applying the inverse Radon transform, the pressure distribution at the measurement time is reconstructed point-wise from the projection data. In the second step, one solves a final time wave inversion problem where the initial pressure distribution is recovered from the known pressure distribution at the measurement time. For the latter problem, we derive an iterative solution approach, compute the required adjoint operator, and show its uniqueness and stability.

1 Introduction

Photoacoustic tomography (PAT) is a hybrid imaging modality that combines high spatial resolution of ultrasound and high contrast of optical tomography [3, 24, 47, 46, 49]. In PAT, a semitransparent sample is illuminated by a short laser pulse. As a result, parts of the optical energy are absorbed inside the sample. This causes an initial pressure distribution and a subsequent acoustic pressure wave. The pressure wave is detected outside the investigated object and used to recover an image of the interior.

In standard PAT, the induced waves are measured on a surface enclosing the investigated object. In the case of constant sound speed and when the observation surface exhibits a special geometry (planar, cylindrical, spherical), initial pressure distribution can be recovered by closed-form inversion formulas; see [1, 8, 10, 11, 17, 13, 14, 16, 23, 26, 28, 29, 27, 48, 49] and references therein. All these algorithms assume that the acoustic pressure is known point-wise on a detection surface. Due to finite width of the commonly used piezoelectric elements this assumption is only approximately satisfied. Therefore, the concept of integrating detectors has been invented as an alternative approach to PAT. Integrating detectors measure the integral of acoustic pressure over planes, lines or circles. Closed-form inversion formulas that incorporate integrated pressure data have been developed in [5, 12, 38, 50].

Inspired by the concept of integrating line detectors, a full field detection method that is capable to image the whole acoustic field around an object has been invented in [36, 37]. In full field detection PAT (FFD-PAT), a phase contrast method is used to obtain data in the form of 2D projections of the pressure field at a time instant T. If the measurement time T is sufficiently large, then the acoustic pressure has essentially left the object. As shown in [36, 37], in the case of constant sound speed, projection data from different directions allow for a full 3D reconstruction of the initial pressure by Radon or Fourier transform techniques.

Existing image reconstruction methods for FFD-PAT assume a constant speed of sound. However, there are relevant cases when the assumption of constant speed of sound is inaccurate [22, 25]. For example, it is known that acoustic properties vary within female human breasts. Consequently, for accurate image reconstruction, variable speed of sound has to be incorporated in the wave propagation model. Iterative methods are capable to deal with this assumption. In the case of standard PAT, such methods have been studied in [2, 4, 15, 20, 35, 42]. Therein the spatially variable speed of sound is assumed to be a smooth function and bounded from below. Moreover, it is assumed to satisfy the so called nontrapping condition, which means that the supremum of the lengths of all geodesics connecting any two points inside the volume enclosed by the measurement surface S is finite. Under this assumption, it is known that the initial pressure can be stably reconstructed from pressure data restricted to $S \times [0, T]$ provided that the measurement time T is sufficiently large.

In this paper, we study image reconstruction in FFD-PAT with a spatially variable speed of sound. We will give a precise mathematical formulation of FFD-PAT and describe the inverse problem we are dealing with (see Section 2). For its solution

we propose a two-step process. In the first step, the acoustic pressure at time T is reconstructed pointwise from the full field data. In the second step, we recover the desired initial pressure from the pressure known for fixed measurement time T. The first step can be approximated by inverting the well-known Radon transform. The second step consists in a final time wave inversion problem with spatially varying speed of sound. To the best of our knowledge, the latter has not been addressed in the literature so far. For its solution, we develop iterative reconstruction methods based on an explicit computation of an adjoint problem. As main theoretical results, we establish uniqueness and stability of the final time wave inversion problem. In particular, this implies linear convergence for the proposed iterative reconstruction methods.
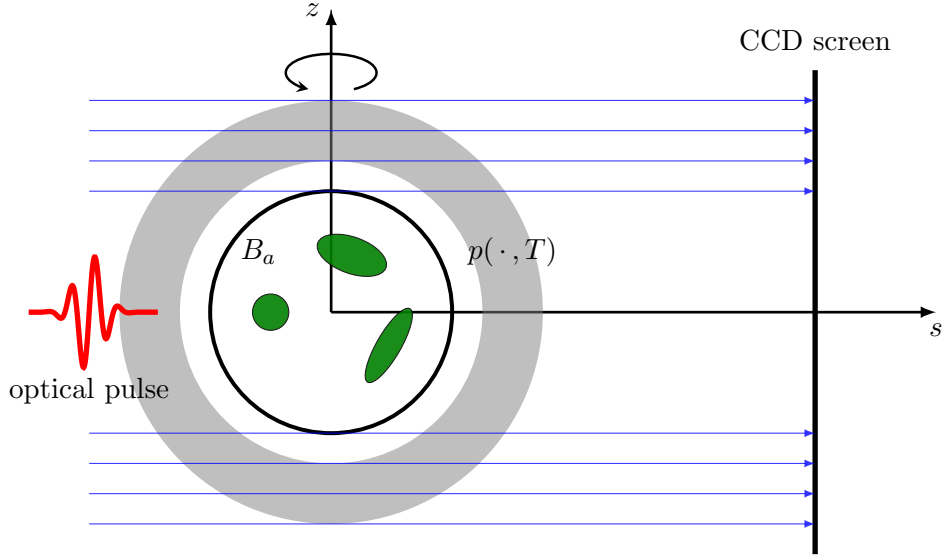

Figure 1.1: **Illustration of FFD-PAT with variable speed of sound.** An object is illuminated by a short pulse of electromagnetic radiation at $t = 0$. After a sufficiently large time $T > 0$, the acoustic pressure $p(\,\cdot\,, T)$ has almost left the investigated object and linear projections of $p(\,\cdot\,, T)$ along lines not intersecting B_a and perpendicular to the CCD screen are recorded. After that, the object is rotated around the $(0, 0, 1)$ axis and the measurement process is repeated.

2 Full field detection photoacoustic tomography

In this section, we describe a mathematical model for FFD-PAT including variable sound speed case, and state the inverse problem under consideration. Additionally, we outline the proposed two-step reconstruction procedure and formulate the final time inverse problem.

2.1 Mathematical model

In the case of variable sound speed, acoustic wave propagation in PAT is commonly described by the widely accepted model [15, 42, 20, 22]

$$p_{tt}(\mathbf{x}, t) - c^2(\mathbf{x})\Delta p(\mathbf{x}, t) = 0, \qquad (\mathbf{x}, t) \in \mathbb{R}^3 \times \mathbb{R}_{>0} \qquad (2.1)$$

$$p(\mathbf{x}, 0) = f(\mathbf{x}), \qquad \mathbf{x} \in \mathbb{R}^3 \qquad (2.2)$$

$$p_t(\mathbf{x}, 0) = 0, \qquad \mathbf{x} \in \mathbb{R}^3. \qquad (2.3)$$

Here $c(\mathbf{x}) > 0$ is the sound speed at location $\mathbf{x} \in \mathbb{R}^3$, and $f \in C_0^\infty(\mathbb{R}^3)$ is the initial pressure distribution that encodes the inner structure of the object. Throughout this text it is assumed that the object is contained inside $B_a = \{\mathbf{x} \in \mathbb{R}^3 \mid \|\mathbf{x}\| < a\}$, the ball of radius a centered at the origin and that the sound speed is smooth, positive and has the constant value c_0 outside B_a.

In FFD-PAT, linear projections (integrals along straight lines) of the 3D pressure field $p(\,\cdot\,, T)$ for a fixed time $T > 0$ are recorded; compare Figure 1.1. This can be implemented using a special phase contrast method and a CCD-camera that recorders full field projections of the pressure field [36, 37]. The projections are collected for rotation angles $\alpha \in [0, \pi]$ around the $e_3 = (0, 0, 1)$ axis and are given by

$$g_a(\alpha, s, z) = \int_{\mathbb{R}} p(s\cos(\alpha) - t\sin(\alpha), s\sin(\alpha) + t\cos(\alpha), z, T)\, dt$$

$$\text{for } (\alpha, s, z) \in M_a := \{(\alpha, s, z) \in [0, \pi] \times \mathbb{R}^2 \mid s^2 + z^2 \geq R^2\}. \quad (2.4)$$

Here M_a determines the set of admissible projections, where the defining condition $s^2 + z^2 \geq R^2$ means that in practice only pressure integrals over those lines are recorded, which do not intersect the possible support of the imaged object.

2.2 Description of the inverse problem

In order to describe the inverse problem of FFD-PAT in a more compact way we introduce some further notation. First, we define the operator

$$\mathbf{A} \colon C_0^\infty(B_a) \to C_0^\infty(\mathbb{R}^3) \colon f \mapsto p(\,\cdot\,, T)\,, \qquad (2.5)$$

where p denotes the solution of (2.1)–(2.3) with initial data f. The operator $\mathbf{A}$ maps the initial data f to the solution (full field) of the wave equation (2.1) at the given measurement time $T > 0$. Second, we define the operator

$$\mathbf{R} \colon C_0^\infty\left(\mathbb{R}^3\right) \to C_0^\infty\left([0, \pi] \times \mathbb{R}^2\right)$$
$$(\mathbf{R}h)(\alpha, s, z) := \int_{\mathbb{R}} h(s\cos(\alpha) - t\sin(\alpha), s\sin(\alpha) + t\cos(\alpha), z)\, dt \qquad (2.6)$$

Note that for any fixed $z \in \mathbb{R}$, the function $(\mathbf{R}h)(\,\cdot\,, z)$ is the Radon transform of $h(\,\cdot\,, z)$ in the horizontal plane $\mathbb{R}^2 \times \{z\}$. Finally, we define the restricted Radon transform

$$\mathbf{R}_a \colon C_0^\infty\left(\mathbb{R}^3\right) \to C^\infty\left(M_a\right) : h \mapsto (\mathbf{R}h)|_{M_a}\,, \qquad (2.7)$$
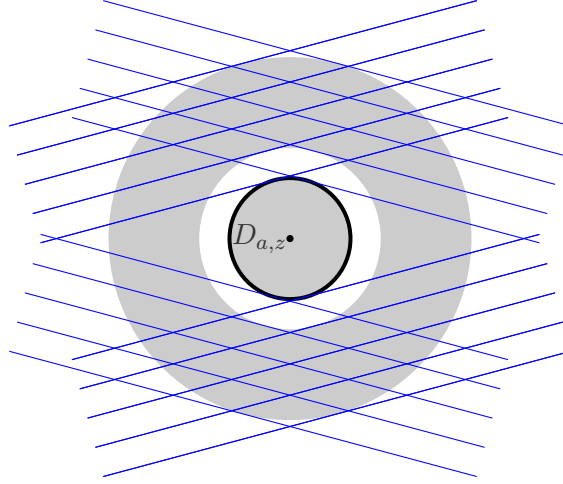
4

Figure 2.1: By measuring full field projections over lines that do not intersect the ball B_a, for any plane $\mathbb{R}^2 \times \{z\}$, integrals of $p(\,\cdot\,, T)$ over lines all lines in $\mathbb{R}^2 \times \{z\}$ are measured that not intersect the disc $D_{a,z} := B_a \cap (\mathbb{R}^2 \times \{z\})$. For $|z| > R$, this yields the exterior problem for the Radon transform.

where M_a is defined in (2.4). For $|z| \leq R$, $(\mathbf{R}_a h)(\,\cdot\,, z)$ is the exterior Radon transform of $h(\,\cdot\,, z)$ for lines not intersecting $\{(x, y) \in \mathbb{R}^2 \mid x^2 + y^2 < R^2 - z^2\}$; compare Figure 2.1. Otherwise, $(\mathbf{R}_a h)(\,\cdot\,, z)$ coincides with the standard Radon transform of $h(\,\cdot\,, z)$.

Using the operator notation introduced above we can write the inverse problem of FFD-PAT in the form

$$\text{Recover } f \text{ from data} \quad g_a = \mathbf{R}_a \mathbf{A} f \,. \tag{2.8}$$

Evaluation of $\mathbf{R}_a \mathbf{A} f$ will be referred to as the forward problem in FFD-PAT. In this paper we study the solution of the inverse problem (2.8).

2.3   Two stage reconstruction

One possible approach to solve the inverse problem of FFD-PAT is to directly recover f from data in (2.8) via iterative methods. Typically, each iteration step will require the evaluation of $\mathbf{R}_a \mathbf{A}$ and $(\mathbf{R}_a \mathbf{A})^* = \mathbf{A}^* \mathbf{R}_a^*$. In this paper, we consider a two-step approach where we first invert $\mathbf{R}_a$ via direct method and then use an iterative method to invert $\mathbf{A}$. This avoids repeated and time consuming evaluation of $\mathbf{R}_a$ and its adjoint.

The proposed two stage reconstruction method consists of the following:

- **Inverse Radon transform:** In this first reconstruction step, assume that projection data $g_a = \mathbf{R}_a \mathbf{A} f$ are given. Assuming $T > 0$ to be sufficiently large, we consider the extension $g \colon [0, \pi] \times \mathbb{R}^2 \to \mathbb{R}$ by $g(\alpha, x, z) = g_a(\alpha, x, z)$ for $(\alpha, x, z) \in M_a$ and $g(\alpha, x, z) = 0$ otherwise. We then define an approximation

5

to $\mathbf{A}f$ by applying an inversion formula of the Radon transform in planes $\mathbb{R}^2 \times \{z\}$. Here we use the well-known filtered backprojection formula (see [31]) which yields

$$\mathbf{A}f(x,y,z) \simeq \mathbf{R}^\sharp g(x,y,z) := \frac{1}{2\pi^2} \int_0^\pi \text{P.V.} \int_{\mathbb{R}} \frac{(\partial_s g)(\alpha, s, z)ds}{(x\cos(\alpha) + y\sin(\alpha)) - s} d\alpha,$$

where P.V. denotes the principal value integral.

■ **Final time wave inversion:** For the second step we assume that an approximation $h \simeq \mathbf{A}f$ to the 3D acoustic field at time T is given. This yields the final time wave inversion problem

$$\text{Recover } f \text{ from data} \quad \mathbf{A}f = h. \quad (2.9)$$

To the best of our knowledge, the problem has not been considered so far and its investigation will be the main theoretical focus of this work.

For solving the wave inversion problem (second step), we propose iterative solution methods that are described in detail in Section 3. Additionally, in Section A.1 we derive uniqueness and stability results for (2.9).

Another option for solving the first step would be to work with the exterior Radon transform [40, 41, 26]. However, we work with the standard Radon transform after replacing the missing values of $\mathbf{R}\mathbf{A}f$ by zero, since they are approximately zero for large enough T. Theoretically, the smallness is supported by the following two facts. First, in the case of non-trapping sound speed the the known decay estimate for the solution of (2.1) states that the following.

Lemma 2.1 (Decay estimate [45]). *Assume that the sound speed c is non-trapping and the initial data f is supported in B_a. Then, for any $(k,m) \in \mathbb{N}^2$, the solution p of (2.1)–(2.3) satisfies*

$$\left| \frac{\partial^{k+|m|} p(\mathbf{x}, t)}{\partial_t^k \partial_{\mathbf{x}}^{|m|}} \right| \leq C e^{-\delta t} \|f\|_2 \quad \text{for } (\mathbf{x}, t) \in B_a \times (T, \infty). \quad (2.10)$$

Here $\delta > 0$ is a constant only depending c and T, and C is a constant depending on the domain B_a.

Second, in the case of constant sound speed, the Radon transform $\mathbf{R}$ reduces the initial value problem (2.1) to a two dimensional wave equation with initial data $\mathbf{R}f$ which is supported in a disc of radius a. As the sound speed is assumed to be constant outside of B_a in the constant sound speed case, $\mathbf{R}\mathbf{A}f$ rapidly decays in the complement of M_a. For non-trapping sound speed we numerically observed the same behaviour. Theoretically investigating this issue, however, is an open problem.

3 Final time wave inversion problem

In this section we study the final time wave inversion problem (2.9), where the forward operator $\mathbf{A}\colon f \mapsto p(\,\cdot\,, T)$ is defined in (2.5). According to standard results

6

for the wave equation [44] the forward operator extends to a bounded linear operator $\mathbf{A}\colon L^2(B_a) \to L^2(\mathbb{R}^3)$. Below we establish uniqueness and stability results and derive an iterative reconstruction algorithm using the CG method.

For constant sound speed, recovering the function f from the solution at time T of (2.1) with initial data $(0, f)$ instead of $(f, 0)$ is equivalent to the the inversion from spherical means at fixed radius. Uniqueness and in inversion method for this problem has been obtained in the classical book of Fritz John [21]. Neither for that case of initial data $(f, 0)$ nor in the variable sound speed case we are not aware of related results.

3.1 Uniqueness and stability

The following theorem is the main theoretical result of this paper and states that the final time wave inversion problem (2.9) has a unique solution that stably depends on the right-hand side.

Theorem 3.1. *The operator* $\mathbf{A}\colon L^2(B_a) \to L^2(\mathbb{R}^3)$ *is injective and bounded from below.*

The proof of Theorem 3.1 is presented in Appendix A.1. It states that

$$b := \inf \left\{ \frac{\|\mathbf{A}f\|_{L^2(\mathbb{R}^3)}}{\|f\|_{L^2(B_a)}} \,\middle|\, f \in L^2(B_a) \right\} > 0 \,. \tag{3.1}$$

In particular, $\mathbf{A}\colon L^2(B_a) \to R(\mathbf{A})$ has a bounded inverse, where $R(\mathbf{A})$ denotes the range of $\mathbf{A}$. The latter result implies that standard iterative methods for (2.9) converge linearly, similar to the case of standard PAT [15].

3.2 Solution by the CG method

To find a solution of (2.9) we use the conjugate gradient (CG) method applied to the normal equation $\mathbf{A}^*\mathbf{A}f = \mathbf{A}^*h$. The CG method has proven to be an accurate and fast reconstruction method for the PAT with variable sound speed [15]. Our numerical experiments confirm that the CG method is also efficient for FFD-PAT, where it reads as follows.

Algorithm 3.2 (CG method for FFD-PAT)**.**

(S1) Initialize: $k = 0$, $r_0 = h - \mathbf{A}f_0$, $d_0 = \mathbf{A}^*r_0$

(S2) While (not stop) do

- $\alpha_k = \|\mathbf{A}^*r_k\|^2 / \|\mathbf{A}d_k\|^2$
- $f_{k+1} = f_k + \alpha_k d_k$
- $r_{k+1} = r_k - \alpha_k \mathbf{A}d_k$

7

$$\blacksquare \quad \beta_k = \|\mathbf{A}^* r_{k+1}\|^2 / \|\mathbf{A}^* r_k\|^2$$

$$\blacksquare \quad d_{k+1} = \mathbf{A}^* r_{k+1} + \beta_k d_k.$$

Using the injectivity and boundedness of $\mathbf{A}$, Algorithm 3.2 generates a series of iterates f_k that converge to the unique solution of the inverse source problem (2.9). The stability of (2.9) even implies that the CG method for FFD-PAT converges linearly. More precisely, the sequence $(f_k)_{k \in \mathbb{N}}$ generated by Algorithm 3.2 satisfies the estimate (see [7])

$$\forall k \in \mathbb{N} \quad \|f_k - f\|_2 \leq 2 \frac{\|\mathbf{A}\|}{b} \left(\frac{\|\mathbf{A}\| - b}{\|\mathbf{A}\| + b} \right)^k \|f_0 - f\|_2^2,$$

where b is defined in (3.1).

3.3 The adjoint operator

The CG method requires knowledge of the adjoint operator $\mathbf{A}^* \colon L^2(\mathbb{R}^3) \to L^2(B_a)$ of $\mathbf{A}$. We show that the adjoint operator is again determined by the solution of a wave equation. More precisely, we have the following result:

Theorem 3.3. *Let $g \in C_0^\infty(\mathbb{R}^3)$, consider the time reversed final state problem for the wave equation,*

$$\begin{aligned} q_{tt}(\mathbf{x}, t) - c(\mathbf{x})^2 \Delta q(\mathbf{x}, t) &= 0, & (\mathbf{x}, t) &\in \mathbb{R}^3 \times (-\infty, T) \\ q(\mathbf{x}, T) &= g(\mathbf{x}), & \mathbf{x} &\in \mathbb{R}^3 \\ q_t(\mathbf{x}, T) &= 0 & \mathbf{x} &\in \mathbb{R}^3, \end{aligned} \tag{3.2}$$

and let χ_{B_a} denote the indicator function of B_a. Then,

$$\mathbf{A}^* g = \chi_{B_a}(\,\cdot\,) q(\,\cdot\,, 0). \tag{3.3}$$

Proof. It is clearly sufficient to show $\mathbf{A}^* g = \chi_{B_a} u_t(\,\cdot\,, 0)$, where u solves the wave equation $u_{tt}(\mathbf{x}, t) - c(\mathbf{x})^2 \Delta c(\mathbf{x}, t) = 0$ on $\mathbb{R}^3 \times (-\infty, T)$, with the final state given by $(u(\,\cdot\,, T), u_t(\,\cdot\,, T)) = (0, f)$. Using the weak formulation (similar to [15]) for the wave equation shows that for every $v \in C_0^\infty(\mathbb{R}^3)$ we have

$$\int_0^T \int_{\mathbb{R}^3} \frac{1}{c^2(\mathbf{x})} u_{tt}(\mathbf{x}, t) v(\mathbf{x}, t) \, d\mathbf{x} dt + \int_0^T \int_{\mathbb{R}^3} \nabla u(\mathbf{x}, t) \cdot \nabla v(\mathbf{x}, t) \, d\mathbf{x} dt = 0.$$

Two times integration by parts, rearranging terms and using the final state conditions $(u(\,\cdot\,, T), u_t(\,\cdot\,, T)) = (0, f)$ yields

$$\int_{\mathbb{R}^3} \frac{1}{c^2(\mathbf{x})} \left[f(\mathbf{x}) v(\mathbf{x}, T) - u_t(\mathbf{x}, 0) v(\mathbf{x}, 0) + u(\mathbf{x}, 0) v_t(\mathbf{x}, 0) \right] d\mathbf{x}$$

$$= \int_0^T \int_{\mathbb{R}^3} u(\mathbf{x},t) \left[c^{-2}(\mathbf{x}) v_{tt}(\mathbf{x},t) - \Delta v(\mathbf{x},t) \right] d\mathbf{x} dt.$$

By taking v as the solution of (2.1)–(2.3) this yields

$$\int_{\mathbb{R}^3} \frac{1}{c^2(\mathbf{x})} g(\mathbf{x}) \, \mathbf{A}(f)(\mathbf{x}) d\mathbf{x} = \int_{\mathbb{R}^3} \frac{1}{c^2(\mathbf{x})} u_t(\mathbf{x},0) f(\mathbf{x}) d\mathbf{x}.$$

This implies $\mathbf{A}^* g = \chi_{B_a} u_t(\,\cdot\,,0) = \chi_{B_a} q(\,\cdot\,,0)$ and completes the proof. $\qquad\square$

We can reformulate the adjoint operator as follows

Corollary 3.4. *For $g \in C_0^\infty(\mathbb{R}^3)$, let q be the solution of*

$$\begin{aligned} q_{tt}(\mathbf{x},t) - c(\mathbf{x})^2 \Delta q(\mathbf{x},t) &= 0, & (\mathbf{x},t) &\in \mathbb{R}^3 \times (0,\infty) \\ q(\mathbf{x},0) &= g(\mathbf{x}), & \mathbf{x} &\in \mathbb{R}^3 \\ q_t(\mathbf{x},0) &= 0 & \mathbf{x} &\in \mathbb{R}^3. \end{aligned} \tag{3.4}$$

Then $\mathbf{A}^* g = \chi_{B_a}(\,\cdot\,) q(\,\cdot\,,T).$

Proof. Clearly q solves (3.4) if and only if $(x,t) \mapsto q(x,T-t)$ solves (3.2). Therefore the claim follows from Theorem 3.3. $\qquad\square$

4 Numerical experiments

In this section we present details on the implementation of CG method (Algorithm 3.2) for FFD-PAT, where the forward operator $\mathbf{A}$ and its adjoint $\mathbf{A}^*$ given by the solution of (2.9) and (3.2), respectively. Numerical experiments are conducted for two variable and two trapping speed of sound models.
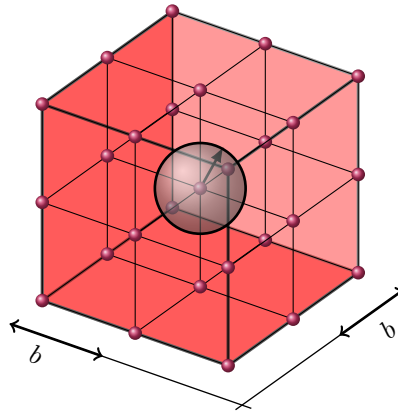

Figure 4.1: The ball B_a is considered to be contained inside a discrete 3D cubic region. The side length l of the cube is chosen to be larger than $4R$ in order to contain the full field $p(\,\cdot\,,T)$.

4.1 Discretization and data simulation

To implement the CG method, we have to discretize $\mathbf{A}$ and its adjoint $\mathbf{A}^*$. For that purpose we solve the forward and adjoint wave equation (2.9) and (3.2) on a cubical grid with nodes

$$\mathbf{x}_{i_1,i_2,i_3} := -(b,b,b) + \frac{2b}{N}(i_1,i_2,i_3) \quad \text{for } (i_1,i_2,i_3) \in \{0,\dots,N-1\}.$$

For the solution (2.9) and (3.2) we use the k-space method [6, 32], which we briefly explain it in Appendix A.2. The implementation of the k-space method yields a $2b$ periodic solution. The parameter b is selected sufficiently large such that the solution of the wave equation (2.1) with initial data supported in B_a coincides with its $2b$-periodic extension for all times $t \in [0, 2T]$; compare Figure 4.1.

We denote by $X_N \subseteq \mathbb{R}^{N \times N \times N}$ the set of all $\mathbf{f}$ with $\mathbf{f}_{i_1,i_2,i_3} = 0$ for $\mathbf{x}_{i_1,i_2,i_3} \notin B_a$. The discretized versions of $\mathbf{A}$ and its adjoint $\mathbf{A}^*$ are defined by

$$\mathbf{A}_{N,M} \colon X_N \to \mathbb{R}^{N \times N \times N} \colon \mathbf{f} \mapsto \mathbf{W}_{N,M}\mathbf{f}(\,\cdot\,, M)$$
$$\mathbf{A}_{N,M}^{\mathsf{T}} \colon \mathbb{R}^{N \times N \times N} \to X_N \colon \mathbf{g} \mapsto \chi_{B_N}\mathbf{W}_{N,M}\mathbf{g}(\,\cdot\,, M).$$

Here $\mathbf{W}_{N,M} \colon \mathbb{R}^{N \times N \times N} \to \mathbb{R}^{N \times N \times N \times (M+1)}$ denotes the discretized wave propagation defined by the k-space method using the discrete time steps jT/M for $0 \le j \le M$.

The discrete and inverse Radon transforms $\mathbf{R}$ and $\mathbf{R}^\sharp$ are computed by the standard MATLAB implementation of the Radon transform and its inverse.

4.2 Sound speed models and phantom

In our numerical setup, we use four different variable sound speed models (A, B, C and D) which are shown in Figure 4.2. All variable sound speed models deviate within 30% from the background sound speed $c_0 = 1$. The two speed of sound models A and B (shown in the upper row) are acoustically non-trapping whereas the speed of sound models C and D (shown the bottom row) are trapping. The speed of sound models A and B have the form

$$c(\mathbf{x}) = 1 + \chi_{B_a}(\mathbf{x}) \sum_{j=1}^{m} e^{-\alpha_m|\mathbf{x}-\mathbf{y}_j|^2}, \tag{4.1}$$

where a sum of Gaussian pulses centered at $\mathbf{y}_j$ added to the background sound speed. The first non-trapping speed of sound model A consists of several pulses with small width, whereas the second model B is a single pulse with a very large width.

In the trapping case C we consider a cavity in the middle of region B_a, which is the difference of the constant speed of sound with a Gaussian pulse. The sound speed D of sound is of the type

$$c(\mathbf{x}) = \begin{cases} 1 + \beta \sin\left(\alpha|\mathbf{x}|^2\right) & \mathbf{x} \in B_a \\ 1 & \mathbf{x} \notin B_a. \end{cases}$$
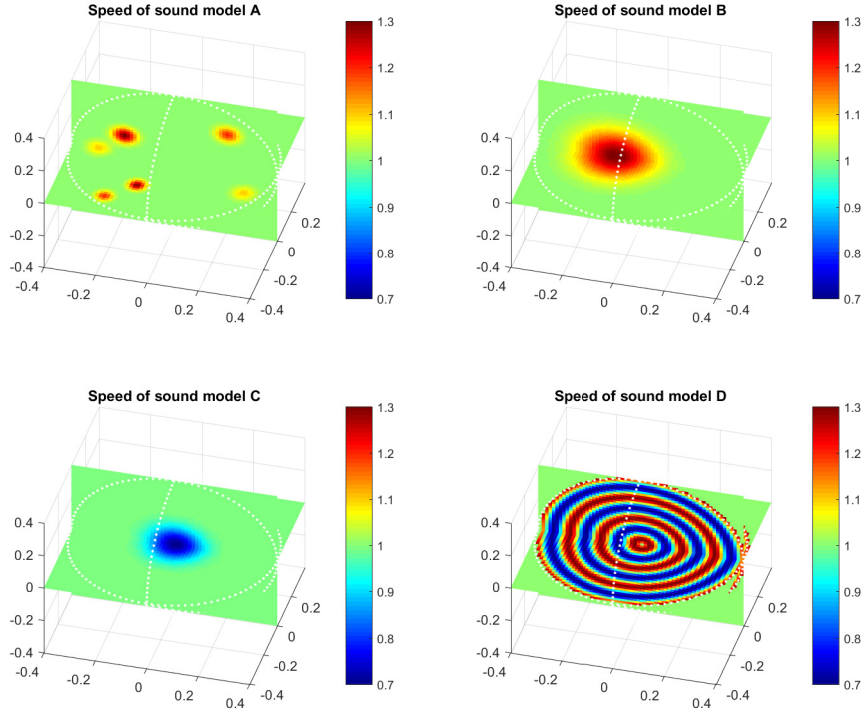
10

Figure 4.2: Top Row: Non-trapping variable speed of sound cases A and B. Bottom row: Trapping speed of sound cases C and D. All cases are assumed to be distortions of the constant background speed of sound $c_0 = 1$.

Since in cases C and D, c is radially symmetric circles concentric to the origin are closed geodesics that never leave B_a. Therefore, this sound speed cases serve as an test case for a trapping speed of sound.

We assume the sum of three solid spheres as initial pressure f, which is depicted in Figure 4.3. The initial pressure distribution is contained inside the B_a of radius $a = 0.4$. In all the experiments we choose $T = 1.4$ and take $b = 2$.

4.3 Pressure simulation

Figure 4.4 shows a slice of the numerically simulated data pressure at $z = 0$ for the different speed of sound models A-D. The simulations show that in the trapping speed of sound case pressure also decreases inside B_a but at a slower rate. Figure 4.5 shows full field data $g_a = \mathbf{R}_a p(\,\cdot\,, T)$ for $z = 0$ and the different speed of sound models, which are the exterior Radon transform of $p(\,\cdot\,, T)$ restricted to the xy-plane. In the first three pictures, we see that the Radon transform almost vanishes in the complement of M_a.
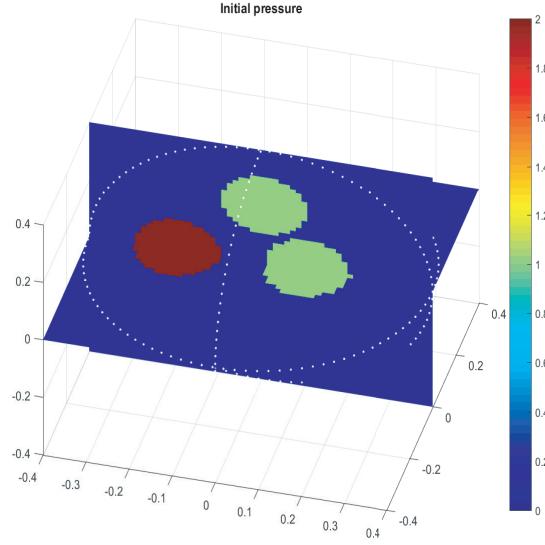
Figure 4.3: Initial pressure f contained in B_a with $a = 0.4$ used for the presented numerical results.

4.4 Application of the CG method

Figure 4.6 shows reconstructions of the pressure fields in the $xy-$plane from the sinograms depicted Figure 4.5. As expected the pressure fields are reconstructed very accurately in the case of a non-trapping speed of sound.

Once point-wise data $p(\,\cdot\,,T)$ are approximated on $\mathbb{R}^3$ we use the CG method outlined in section 3 to numerically compute the initial pressure f of system (2.1)–(2.3). Figure 4.7 shows slice images of the initial pressure corresponding to the different sound speed cases after four iterations of the CG method.

As expected reconstructions are better for the non-trapping speed of sound models. Figure 4.8 shows the output of the algorithm after one iteration. Finally, Figure 4.9 shows the reconstruction result, when a wrong speed of sound (namely constant value 1) is used. From this we can clearly see that not accounting for variable speed can introduce a significant error.

5 Conclusion

In this paper, we described a FFD-PAT method, where projection data of acoustic pressure are measured. For the first time, we consider this method for variable speed of sound. We developed a two-step reconstruction procedure that computes 3D acoustic pressure data point-wise in a first step and then uses them as input for an iterative algorithm in a second step. We prove uniqueness and stability estimates for the second step. Furthermore, in upcoming works we will also study
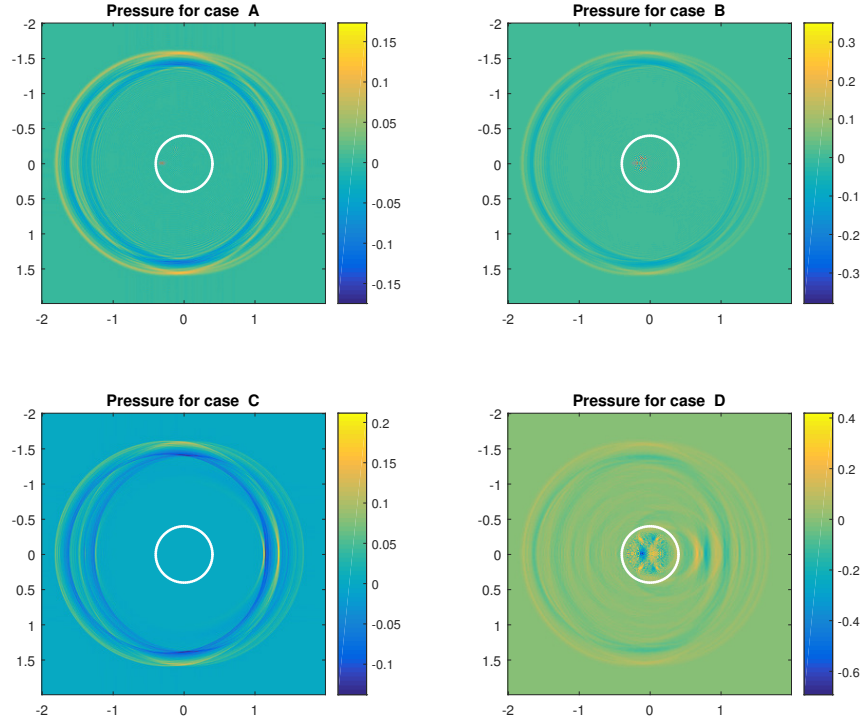
Figure 4.4: Slice of $\mathbf{A}f = p(\,\cdot\,, T)$ through the plane $z = 0$ for the sound speed models A-D.

additional limited view problems for FFD-PAT which naturally arise in applications, for instance in the case of breast imaging.

Acknowledgement

A   Appendix

A.1   Uniqueness and stability

Let us prove Theorem 3.1. To that end, we first prove two crucial results.

Proposition A.1. *Assume that* $p(\,\cdot\,, T) = 0$*, then* $f \equiv 0$*. That is,* $\mathbf{A}$ *is injective.*
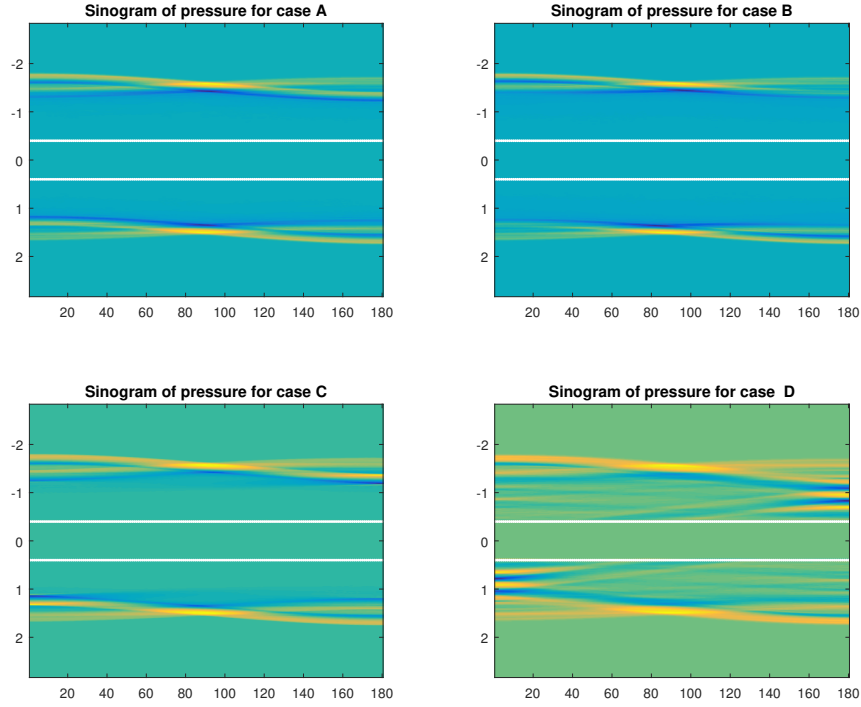
13

Figure 4.5: Simulated data $\mathbf{R}_a\mathbf{A}f$ at $z = 0$ for sound speed models A-D. Values between the white lines (determined by the set M_a) extended are zero.

Proof. Let us construct a solution $\bar{p}$ of the wave equation which is periodic in time with period $4T$ such that $\bar{p} = p$ on $\mathbb{R}^3 \times [0, T]$. Once this is done, we obtain $f = \bar{p}(\,\cdot\,, 0) = \bar{p}(\,\cdot\,, 4^n T)$ for any n. Using Lemma 2.1, we arrive at

$$f(\mathbf{x}) = \lim_{n \to \infty} \bar{p}(\mathbf{x}, 4^n T) = 0, \quad \forall\, \mathbf{x} \in \mathbb{R}^3.$$

It now remains to construct the above-mentioned solution $\bar{p}$ of the wave equation. The idea is to properly reflect the solution p in the time variable t through the time moments $t = T, 2T, \dots$, as follows. We first construct $\bar{p}$ on $[0, 2T]$ by the odd reflection of p through the moment $t = T$: $\bar{p}(\,\cdot\,, T) = p(\,\cdot\,, T)$ for $t \in [0, T]$ and $\bar{p}(\,\cdot\,, T) = -p(\cdot, 2T - t)$ for all $t \in [T, 2T]$. Since $p(\,\cdot\,, T) = 0$ on $\mathbb{R}^3$, we obtain that $\bar{p}$ and $\bar{p}_t$ are continuous at $t = T$. Therefore, p is continuous on $[0, 2T]$ and solves the wave equation on that interval.

We note that $\bar{p}_t(\cdot, 2T) = -\bar{p}_t(\cdot, 0) = 0$ on $\mathbb{R}^3$. By the even reflection through $t = 2T$: $\bar{p}(\,\cdot\,, T) = \bar{p}(\,\cdot\,, 4T - t)$ for all $t \in [2T, 4T]$, we obtain that $\bar{p}$ is a solution of the wave equation in $[0, 4T]$. Finally, we extend the solution by periodicity with period $4T$. Noting that $\bar{p}(\,\cdot\,, 0) = \bar{p}(\,\cdot\,, 4T)$ and $\bar{p}_t(\,\cdot\,, 0) = \bar{p}_t(\,\cdot\,, 4T) = 0$, we obtain that $\bar{p}$ and $\bar{p}_t$ are continuous for all time and $\bar{p}$ satisfies the wave equation in $\mathbb{R}^3 \times \mathbb{R}_+$. This finishes our proof. □
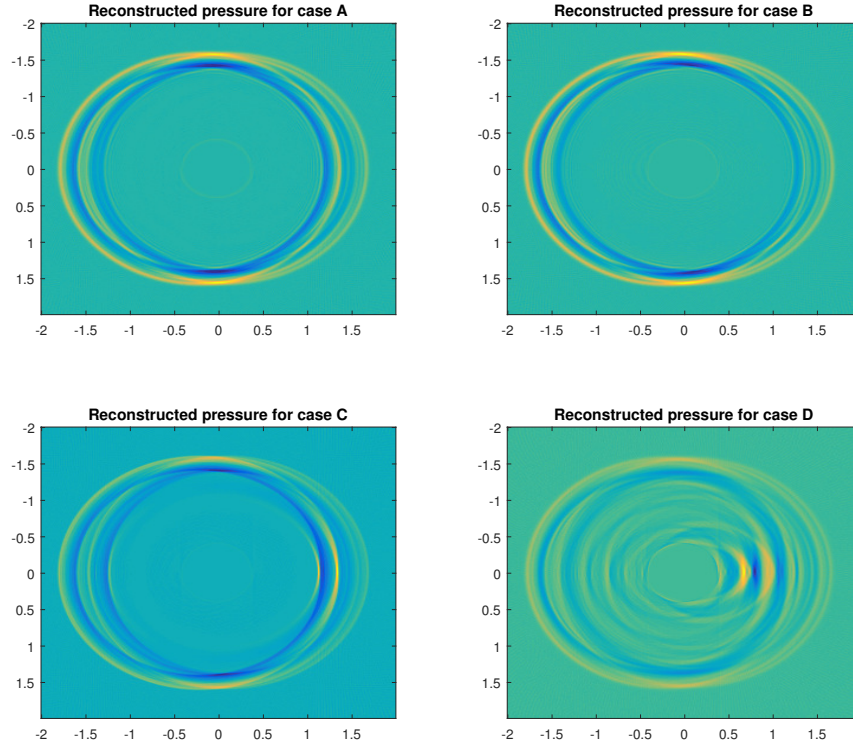
14

Figure 4.6: Slices of the reconstruction of $\mathbf{A}f$ through the plane $z = 0$ by applying $\mathbf{R}^{\sharp}$ for the speed of sound models A-D.

Proposition A.2. *There is a constant C such that*

$$\|f\|_{L^2(\Omega)} \le 2(\|\mathbf{A}f\|_{L^2(\mathbb{R}^3)} + \|Kf\|_{L^2(B_a)}),$$

where K is a pseudo-differential operator of order at most -1.

Proof. Let us recall the parametrix formula for the solution p of the wave equation (2.1)–(2.3) (e.g., [44]):

$$p(\mathbf{y}, t) = \frac{1}{(2\pi)^3} \sum_{\pm} \int_{\mathbb{R}^3} a_{\pm}(\mathbf{y}, t, \xi) e^{i\phi_{\pm}(\mathbf{y}, T, \xi)} \hat{f}(\xi) \, d\xi = \sum_{\pm} p_{\pm}(\mathbf{y}, t).$$

Here, the phase function $\phi_{\pm}$ solves the eikonal equation

$$\partial_t \phi_{\pm}(\mathbf{y}, t, \xi) \pm c(\mathbf{y}) |\nabla_{\mathbf{y}} \phi_{\pm}(\mathbf{y}, t, \xi)| = 0, \quad (\mathbf{y}, t) \in \mathbb{R}^3 \times \mathbb{R}_+$$

with the initial condition

$$\phi_{\pm}(\mathbf{x}, 0, \xi) = \mathbf{x} \cdot \xi.$$

The amplitude function is a classical symbol $a_{\pm}(\mathbf{y}, t, \xi) = \sum_{k=0}^{\infty} a_{-k,\pm}(\mathbf{y}, t, \xi)$, where a_{-k} is homogeneous of order $-k$ in ξ. Its leading term $a_{0,\pm}$ satisfies the transport
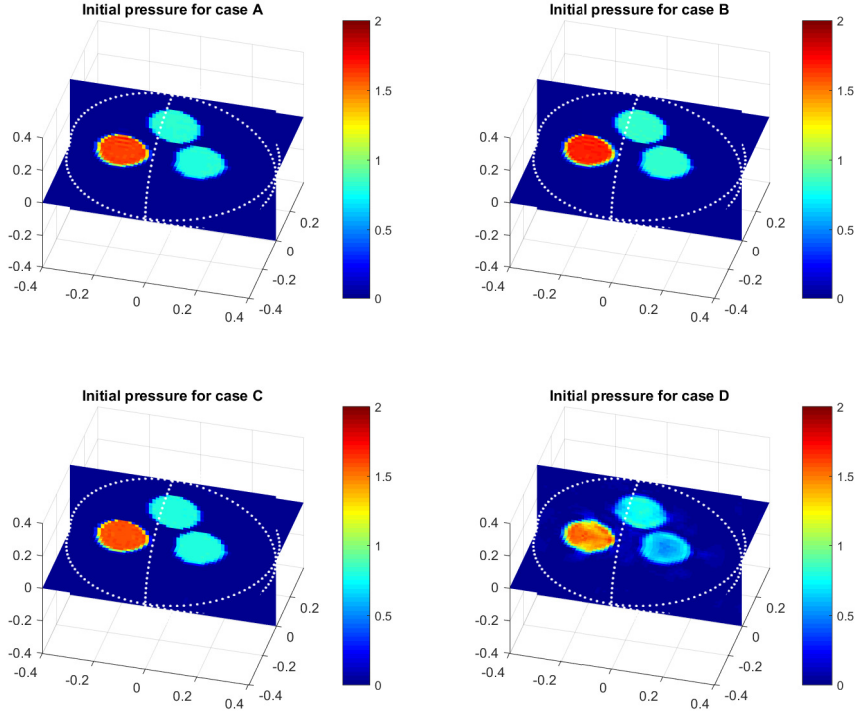
15

Figure 4.7: Reconstructions of the initial after four iterations with the CG algorithm for the speed of sound models A-D.

equation

$$\big(\partial_t \phi_\pm(\mathbf{y}, t, \xi)\partial_t - c^2(\mathbf{y})\nabla_\mathbf{y}\phi_\pm(\mathbf{y}, t, \xi)\cdot\nabla_\mathbf{y} + C_\pm(\mathbf{y}, t, \xi)\big)a_{0,\pm}(\mathbf{y}, t, \xi) = 0, \quad \text{(A.1)}$$

with the initial condition $a_{\pm,0}(\mathbf{x}, 0, \xi) = \frac{1}{2}$ (see [42]). Here, $C(\mathbf{y}, \xi, t)$ only depends on the sound speed c and the phase function $\phi_\pm$. Let us denote by $\gamma_{\mathbf{x},\xi}$ the unit speed geodesics originating at $\mathbf{x}$ along the direction ξ. Then, $\gamma_{\mathbf{x},\xi}$ is a characteristics curve of the above transport equation; that is, (A.1) reduces to a homogeneous ODE on each geodesic curve.

We then write

$$\mathbf{A}(f)(\mathbf{y}) \quad = \quad \frac{1}{(2\pi)^3}\sum_\pm \int_{\mathbb{R}^3} a_\pm(\mathbf{y}, T, \xi)e^{i\phi_\pm(\mathbf{y},T,\xi)}\hat{f}(\xi)\,d\xi = \sum_\pm \mathbf{A}_\pm(f)(\mathbf{y}).$$

Each operator $\mathbf{A}_\pm$ is a Fourier integral operator (FIO) with the canonical relation given by the pairs $(\mathbf{y}_\pm, \lambda\eta_\pm; \mathbf{x}, \lambda\xi)$ for any $\lambda \in \mathbb{R}$, ξ, η unit vectors, $\mathbf{y}_\pm = \gamma_{\mathbf{x},\xi}(\pm T)$, and $\eta_\pm = \dot{\gamma}_{\mathbf{x},\xi}(\pm T)$. Let $\mathbb{R}^3$ be equipped with the metrics $c^{-2}(\mathbf{x})\,d\mathbf{x}^2$. Then, $(\mathbf{y}_\pm, \eta_\pm)$ is obtained by translating $(\mathbf{x}, \xi)$ on the geodesic $\gamma_{\mathbf{x},\pm\xi}$ by the distance T. From the initial condition of $\phi_\pm$ and $a_{0,\pm}$ we see that, up to lower order terms,

$$p_-(\mathbf{x}, 0) = p_+(\mathbf{x}, 0) = \frac{1}{2}f(\mathbf{x}). \quad \text{(A.2)}$$
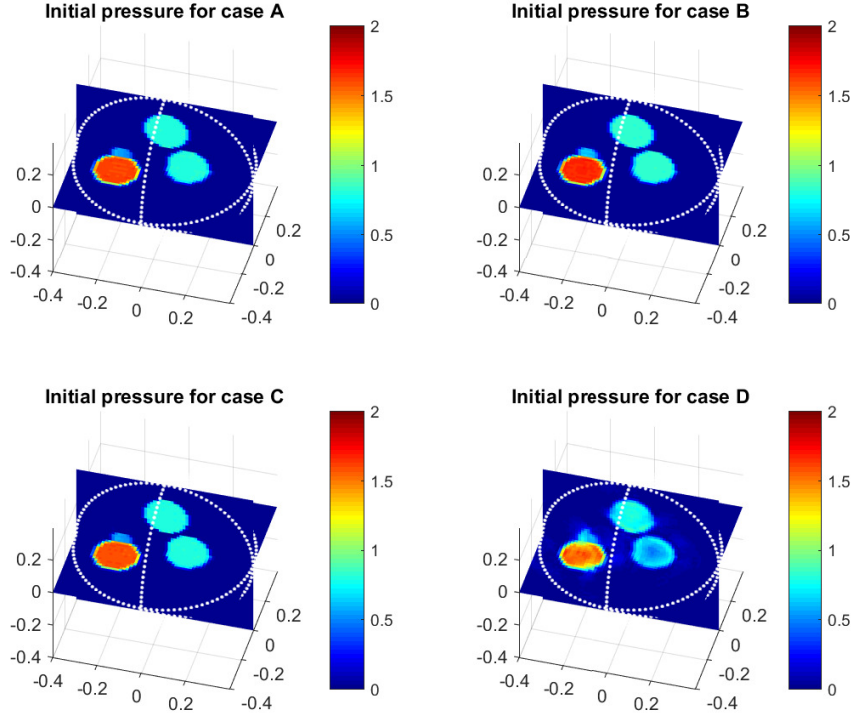
16

Figure 4.8: Reconstructions of the initial after one iteration with the CG algorithm for the speed of sound models A-D.

Heuristically, under equation (2.1)–(2.3), each singularity of f at $(\mathbf{x}, \xi)$ is broken into two equal parts. They propagate along the geodesic $\gamma_{\mathbf{x},\xi}$ in the opposite directions $\pm\xi$ to generate a singularity of $\mathbf{A}(f)$ at $(\mathbf{y}_\pm, \eta_\pm)$.

From the standard theory of FIOs (see [18]), the adjoint $\mathbf{A}_\pm^*$ translates $(\mathbf{y}_\pm, \eta_\pm)$ back to $(\mathbf{x}, \xi)$ and $\mathbf{A}_\pm^* \mathbf{A}_\pm$ is a pseudo differential operator. On the other hand, $\mathbf{A}_\mp^* \mathbf{A}_\pm$ is a FIO whose canonical relation consists of the pairs $(\mathbf{y}, \eta; \mathbf{x}, \xi)$ given by $\mathbf{y} = \gamma_{\mathbf{x},\xi}(\pm 2T)$, and $\eta = \dot{\gamma}_{\mathbf{x},\xi}(\pm 2T)$. That is, $\mathbf{A}_\pm^* \mathbf{A}_\mp$ is an infinitely smoothing operator on B. Therefore, microlocally, we can write

$$\mathbf{A}^* \mathbf{A} f = \mathbf{A}_+^* \mathbf{A}_+(f) + \mathbf{A}_-^* \mathbf{A}_-(f). \tag{A.3}$$

We will show that the principal symbol $\alpha_\pm(\mathbf{x}, \xi)$ of $\mathbf{A}_\pm^* \mathbf{A}_\pm$ satisfies $\alpha_\pm(\mathbf{x}, \xi) = \frac{1}{4}$. This result can be intuitively understood as follows. Let us consider $\mathbf{A}_+^* \mathbf{A}_+$ and a singularity of f at $(\mathbf{x}, \xi)$. Under equation (2.1)–(2.3), half of this singularity propagates into the direction ξ (corresponding to the function p_+). At the moment $t = T$, it is transformed to a singularity of $\mathbf{A}_+(f) = p_+(T)$ at $(\mathbf{y}_+, \eta_+)$. Under the adjoint equation (3.2), half of this singularity propagates back to $(\mathbf{x}, \xi)$ at $t = 0$ to generate a singularity of $\mathbf{A}_+^* \mathbf{A}_+(f)$. It is natural to believe that this recovered singularity is $\frac{1}{4}$ of the original singularity of f (due to twice splitting, as described). The proof below verify this intuition.
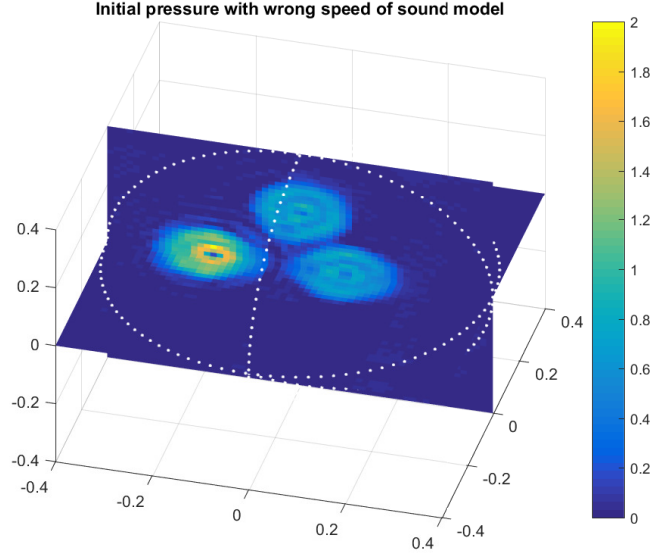
Figure 4.9: Reconstruction of the initial pressure after four iterations, when data are generated with speed of sound model B but the iterative CG algorithm assumes constant speed of sound with value one.

Indeed, denote by q_+ the solution of the time-reversed wave equation, e.g., equation (3.2), with the initial condition given by $g_+ = \mathbf{A}_+(f)$. Then, by definition (see Theorem 3.3) $\mathbf{A}^* g_+ = q_+(\,\cdot\,, 0)|_B$. The solution q_+ can be decomposed into the sum $q_+ = q_0 + q_1$. Here, q_0, q_1, up to smooth terms, are solutions of the wave equations in $\mathbb{R}^3 \times (0, T)$ and satisfy $q_0(\,\cdot\,, 0) = \mathbf{A}^*_+(g_+)$, $q_1(\,\cdot\,, 0) = \mathbf{A}^*_-(g_+)$. We are only concerned with q_0 since it defines $\mathbf{A}^*_+ \mathbf{A}_+ f = q_0(\,\cdot\,, 0)$. We can write

$$q_0(\mathbf{y}, t) = \frac{1}{(2\pi)^3} \int_{\mathbb{R}^3} b(\mathbf{y}, t, \xi) e^{i\phi_+(\mathbf{y}, t, \xi)} \hat{f}(\xi) \, d\xi. \tag{A.4}$$

Let b_0 be the principal part of b. Then, the principal symbol α_+ of $\mathbf{A}^*_+ \mathbf{A}_+$ is given by $\alpha_+(\mathbf{x}, \xi) = b_0(\mathbf{x}, 0, \xi)$. We note that b_0 satisfies the same equation as $a_{0,+}$ (see (A.1)). Therefore, on each bicharacteristic curve the ratio $b_0/a_{0,+}$ is constant. That implies $b_0(\mathbf{x}, 0, \xi) = a_{+,0}(\mathbf{x}, 0, \xi) \frac{b_0(\mathbf{y}_+, T, \eta_+)}{a_{+,0}(\mathbf{y}_+, T, \eta_+)}$. Similarly to the argument below equation (A.2), up to lower order terms, we have

$$q_0(\mathbf{y}_+, T) = \frac{1}{2} g_+(\mathbf{y}_+, T) = \frac{1}{(2\pi)^3} \int_{\mathbb{R}^3} \frac{1}{2} a_+(\mathbf{y}_+, T, \xi) e^{i\phi_+(\mathbf{y}_+, T, \xi)} \hat{f}(\xi) \, d\xi.$$

This and equation (A.4) implies that $b_0(\mathbf{y}_+, T, \xi) = \frac{1}{2} a_{+,0}(\mathbf{y}_+, T, \xi)$. Therefore we obtain

$$b_0(\mathbf{x}, 0, \xi) = \frac{1}{2} a_{+,0}(\mathbf{x}, 0, \xi) = \frac{1}{4}.$$

Combining with a similar argument for $\mathbf{A}^*_- \mathbf{A}_-$, we obtain that the principal symbol of $\mathbf{A}^* \mathbf{A}$ is $\alpha(\mathbf{x}, \xi) = \frac{1}{2}$. That is, $\mathbf{A}^* \mathbf{A} = \frac{1}{2} I + K$, where K is a pseudodifferential operator of order at most -1.

18

Now

$$(\mathbf{A}f, \mathbf{A}f) = (\mathbf{A}^*\mathbf{A}f, f) = \frac{1}{2}(f, f) + (Kf, f).$$

We conclude that

$$\|f\|_{L^2}^2 \leq 2(\|\mathbf{A}f\|_{L^2}^2 + \|Kf\|_{L^2}^2). \quad \square$$

We are now ready to prove Theorem 3.1.

Proof of Theorem 3.1. Let us recall from Proposition A.2

$$\|f\|_{L^2(B_a)} \leq 2(\|\mathbf{A}f\|_{L^2(\mathbb{R}^3)} + \|Kf\|_{L^2(B_a)}),$$

where K is a pseudo-differential operator of order at most -1. Since K is compact and $\mathbf{A}$ is injective, applying [43, Theorem V.3.1], we obtain

$$\|f\|_{L^2(B_a)} \leq C\|\mathbf{A}f\|_{L^2(\mathbb{R}^3)}$$

for some constant $C \in (0, \infty)$. This finishes our proof. $\hfill\square$

A.2 k-space method

We briefly describe the k-space method for the 3D wave equation (2.1)–(2.3) as we use it for the numerical computation of $\mathbf{A}$ and $\mathbf{A}^*$. The k-space method is an attractive alternative to standard methods using finite differences, finite elements or pseudospectral methods, since it does not suffer from numerical dispersion [6, 32]. It utilizes the decomposition $p(\mathbf{x}, t) = w(\mathbf{x}, t) - v(\mathbf{x}, t)$, where v, w are defined by

$$w(\mathbf{x}, t) := \frac{c_0^2}{c^2(\mathbf{x})}\, p(\mathbf{x}, t) \text{ and } v(\mathbf{x}, t) = \left(\frac{c_0^2}{c^2(\mathbf{x})} - 1\right) p(\mathbf{x}, t),$$

where $c_0 := \max\{c(\mathbf{x}) : \mathbf{x} \in \mathbb{R}^3\}$ denotes maximal speed of sound. It can be checked that with this definition of v and w the wave equation with variable speed of sound splits into the system

$$w_{tt}(\mathbf{x}, t) - c_0^2 \Delta w(\mathbf{x}, t) = -c_0^2 \Delta v(\mathbf{x}, t),$$
$$v(\mathbf{x}, t) = \frac{c_0^2 - c(\mathbf{x})^2}{c_0^2} w(\mathbf{x}, t).$$

In the k-space method we use the time stepping formula

$$w(\mathbf{x}, t + h_t) = 2w(\mathbf{x}, t) - w(\mathbf{x}, t - h_t) \tag{A.5}$$

$$- 4\mathbf{F}_\xi^{-1}\left\{\sin\left(\frac{c_0|\xi|h_t}{2}\right)^2 \mathbf{F}_\mathbf{x}\{w(\mathbf{x}, t) - v(\mathbf{x}, t)\} - \left(\frac{c_0 h_t}{2}\right)^2\right\},$$

where $\mathbf{F}_x$ and $\mathbf{F}_\xi^{-1}$ denote the Fourier transform and its inverse with respect to space and frequency variables $\mathbf{x}$ and ξ and h_t is the time step size. This equivalent formulation motivates the following algorithm for numerically solving the wave equation.

19

Algorithm A.3 (*k*-space method for numerically solving (2.1)–(2.3))**.**

(S1) Define initial conditions:

$$w(\mathbf{x}, -h_t) = w(\mathbf{x}, 0) = c_0^2/c^2(\mathbf{x})f(\mathbf{x}),$$
$$v(\mathbf{x}, 0) = (c_0^2/c^2(\mathbf{x}) - 1)f(\mathbf{x})$$

(S2) Set $t = 0$

(S3) Compute $w(\mathbf{x}, t + h_t)$ according to equation (A.5)

(S4) Compute $v(\mathbf{x}, t + h_t) := (c^2(\mathbf{x})/c_0^2 - 1)w(\mathbf{x}, h_t)$

(S5) Compute $p(\mathbf{x}, t + h_t) := w(\mathbf{x}, t + h_t) - w(\mathbf{x}, t + h_t)$

(S6) Substitute t by $t + h_t$ and go back to step (3).

References

[1] M. AGRANOVSKY, P. KUCHMENT, AND L. KUNYANSKY, *On reconstruction formulas and algorithms for the thermoacoustic tomography*, Photoacoustic imaging and spectroscopy, L. V. Wang, ed., CRC Press, 2009, ch. 8, pp. 89–101.

[2] S. R. ARRIDGE, M. M. BETCKE, B. T. COX, F. LUCKA, AND B. E.TREEBY, *On the adjoint operator in photoacoustic tomography*, Inverse Problems 32 (2016), pp. 115012.

[3] P. BEARD, *Biomedical photoacoustic imaging*, Interface Focus 1 (2011), pp. 602–631.

[4] Z. BELHACHMI, T. GLATZ, AND O. SCHERZER, *A direct method for photoacoustic tomography with inhomogeneous sound speed*, Inverse Problems 32 (2016), pp. 045005.

cv

[5] P. BURGHOLZER, J. BAUER-MARSCHALLINGER, H. GRÜN, M. HALTMEIER, AND G. PALTAUF, *Temporal back-projection algorithms for photoacoustic tomography with integrating line detectors*, Inverse Problems 23 (2007), pp. S65–S80.

[6] B. T. COX, S. KARA, S. R. ARRIDGE, AND P. C. BEARD, *k-space propagation models for acoustically heterogeneous media: Application to biomedical photoacoustics.*, J. Acoust. Soc. Am. 121 (2007), pp. 3453–3464.

[7] J. W. DANIEL, *The conjugate gradient method for linear and nonlinear operator equations*, SIAM J. Numer. Anal. 4 (1967), pp. 10–26.

[8] F. FILBIR, S. KUNIS, AND R. SEYFRIED, *Effective discretization of direct reconstruction schemes for photoacoustic imaging in spherical geometries*, SIAM J. Numer. Anal. 52 (2014), pp. 2722–2742.

[9] D. FINCH AND RAKESH, *The spherical mean value operator with centers on a sphere*, Inverse Problems 23 (2007), pp. 37–49.

[10] D. FINCH, M. HALTMEIER, AND RAKESH, *Inversion of spherical means and the wave equation in even dimensions*, SIAM J. Appl. Math. 68 (2007), pp. 392–412.

[11] D. FINCH, S. K. PATCH, AND RAKESH, *Determining a function from its mean values over a family of spheres*, SIAM J. Math. Anal. 35 (2004), pp. 1213–1240.

[12] M. HALTMEIER, O. SCHERZER, P. BURGHOLZER AND G. PALTAUF, *Thermoacoustic computed tomography with large planar receivers*, Inverse Problems 20 (2004), pp. 1663.

[13] M. HALTMEIER, *Universal inversion formulas for recovering a function from spherical means*, SIAM J. Math. Anal. 46 (2014), pp. 214–232.

[14] M. HALTMEIER, *Exact Reconstruction Formula for the Spherical Mean Radon Transform on Ellipsoids*, Inverse Problems 30 (2014), pp. 035001.

[15] M. HALTMEIER, AND L. V. NGUYEN, *Analysis of Iterative Methods in Photoacoustic Tomography with variable Sound Speed*, SIAM J. Imaging Sci. 19 (2017), pp. 751–781.

[16] M. HALTMEIER AND S. PEREVERZYEV, JR., *The universal back-projection formula for spherical means and the wave equation on certain quadric hypersurfaces*, J. Math. Anal. Appl. 429 (2015), pp. 366–382.

[17] M. HALTMEIER, T. SCHUSTER, AND O. SCHERZER, *Filtered backprojection for thermoacoustic computed tomography in spherical geometry*, Math. Method. Appl. Sci. 28 (2005), pp. 1919–1937.

[18] L. HÖRMANDER, *Fourier integral operators. I.*, Acta Math. 127(1) (1971).

[19] Y. HRISTOVA, P. KUCHMENT, AND L. NGUYEN, *Reconstruction and time reversal in thermoacoustic tomography in acoustically homogeneous and inhomogeneous media*, Inverse Problems 24 (2008), pp. 055006.

[20] C. HUANG, K. WANG, L. NIE, L. V. WANG, AND M. A. ANASTASIO, *Full-wave iterative image reconstruction in photoacoustic tomography with acoustically inhomogeneous media*, IEEE Trans. Med. Imag. 32 (2013), pp. 1097–1110.

[21] F. JOHN, *Partial Differential Equations*, vol. 1 of Applied Mathematical Sciences, Springer Verlag, New York, fourth ed., 1982.

[22] X. JIN, L. V. WANG, *Thermoacoustic tomography with correction for acoustic speed variations*, Phys. Med. Biol. 51 (2006), pp. 6437.

[23] R. KOWAR, *On time reversal in photoacoustic tomography for tissue similar to water*, SIAM J. Imaging Sci. 7 (2014), pp. 509–527.

[24] R. A. KRUGER, K. K. KOPECKY, A. M. AISEN, R. D. REINECKE, G. A. KRUGER, AND W. L. KISER, *Thermoacoustic CT with Radio waves: A medical imaging paradigm*, Radiology 200 (1999), pp. 275–278.

[25] G. KU, B. D. FORNAGE, J. XING, M. XU, K. K. HUNT AND L. V. WANG, *Thermoacoustic and photoacoustic tomography of thick biological tissues toward breast imaging*, Med. Phys. 22 (1995), pp. 1605–1609.

[26] P. KUCHMENT, *The Radon transform and medical imaging*, vol. 85, SIAM, 2014.

[27] P. KUCHMENT AND L. A. KUNYANSKY, *Mathematics of thermoacoustic and photoacoustic tomography*, Eur. J. Appl. Math. 19 (2008), pp. 191–224.

[28] L. A. KUNYANSKY, *Explicit inversion formulae for the spherical mean Radon transform*, Inverse Problems 23 (2007), pp. 373–383.

[29] L. A. KUNYANSKY, *A series solution and a fast algorithm for the inversion of the spherical mean Radon transform*, Inverse Problems 23 (2007), pp. S11–S20.

[30] F. NATTERER, *Photo-acoustic inversion in convex domains*, Inverse Probl. Imaging 6 (2012), pp. 315–320.

[31] F. NATTERER, *The mathematics of computerized tomography*, Siam, 1986.

[32] T. D. MAST, L. P. SOURIAU, D-LD. LIU, M. TABEI, A. I. NACHMAN, AND R. C. WAAG, *A k-space method for large-scale models of wave propagation in tissue*, IEEE Trans. Ultrason. Ferroelectr. Freq. Control 48 (2002), pp. 341–354.

[33] L. V. NGUYEN, *On singularities and instability of reconstruction in thermoacoustic tomography*, Tomography and inverse transport theory, Contemp. Math., 559 (2011), pp. 163–170.

[34] L. V. NGUYEN, *A family of inversion formulas for thermoacoustic tomography*, Inverse Probl. Imaging 3 (2009), pp. 649–675.

[35] L. V. NGUYEN AND M. HALTMEIER, *Reconstruction algorithms for photoacoustic tomography in heterogenous damping media*, submitted (2018).

[36] R. NUSTER, G. ZANGERL, M. HALTMEIER AND G. PALTAUF, *Full field detection in photoacoustic tomography*, Opt. Express 18 (2010), pp. 6288–6299.

[37] R. NUSTER, P. SLEZAK AND G. PALTAUF, *High resolution three-dimensional photoacoustic tomography with CCD-camera based ultrasound detection*, Biomed. Opt. Express 5 (2014), pp. 2635-2647.

[38] G. PALTAUF, R. NUSTER AND M. HALTMEIER, *Experimental evaluation of reconstruction algorithms for limited view photoacoustic tomography with line detectors*, Inverse Problems 23 (2007), pp. S81–S94.

[39] X. PAN, E. SIDKY AND M. VANNIER, *Why do commercial CT scanners still employ traditional, filtered back-projection for image reconstruction?*, Inverse Problems 25 (2009), pp. 123009.

[40] E. QUINTO, *Singular value decompositions and inversion methods for the exterior Radon transform and a spherical transform*, J. Math. Anal. Appl. 95 (1983), pp. 437–448.

[41] E. QUINTO, *Tomographic reconstructions from incomplete data-numerical inversion of the exterior Radon transform*, Inverse Problems 4 (1988), pp. 867.

[42] P. STEFANOV AND G. UHLMANN, *Thermoacoustic tomography with variable sound speed*, Inverse Problems 25 (2009), pp. 075011, 16.

[43] M. E. TAYLOR, *Pseudodifferential operators, volume 34 of princeton mathematical series*, 1981.

[44] F. TRÉVES, *Introduction to pseudodifferential and Fourier integral operators Volume 2: Fourier integral operators (Vol. 2)*. Springer Science & Business Media. (1980).

[45] B. VAINBERG, *On the short wave asymptotic behaviour of solutions of stationary problems and the asymptotic behaviour as $t \to \infty$ of solutions of nonstationary problems*, Russian Math. Surveys 30 (1975), pp.1-58.

[46] L. V. WANG, *Multiscale photoacoustic microscopy and computed tomography*, Nat. Photonics 3 (2009), pp. 503–509.

[47] K. WANG AND M. ANASTASIO, *Photoacoustic and thermoacoustic tomography: Image formation principles*, in Handbook of Mathematical Methods in Imaging, Springer, 2011, ch. 18, pp. 781–815.

[48] M. XU AND L. V. WANG, *Universal back-projection algorithm for photoacoustic computed tomography*, Phys. Rev. E 71 (2005), p. 016706.

[49] M. XU AND L. V. WANG, *Photoacoustic imaging in biomedicine*, Rev. Sci. Instrum. 77 (2006), p. 041101.

[50] G. ZANGERL, O. SCHERZER AND M. HALTMEIER, *Exact series reconstruction in photoacoustic tomography with circular integrating detectors*, Commun. Math. Sci. 7 (2009), pp. 665–678.

23